SCIENCE CHINA
Technological Sciences

•Article•

June 2023 Vol.66 No.6: 1734–1745
https://doi.org/10.1007/s11431-022-2362-y

Wide measurement range and high sensitivity spongy MWCNT/polydimethylsiloxane pressure sensor based on a single-electrode enhanced triboelectric nanogenerator

XIE Xin[1], HOU XiaoJuan[1*], QIAN Shuo[2], HOU JianWei[1], ZHANG Jie[1], BI XiaoXue[1], GENG WenPing[1], MU JiLiang[1], HE Jian[1*] & CHOU XiuJian[1]

[1] *Science and Technology on Electronic Test and Measurement Laboratory, North University of China, Taiyuan 030051, China;*
[2] *School of Software, North University of China, Taiyuan 030051, China*

Received November 10, 2022; accepted February 23, 2023; published online May 9, 2023

Flexible pressure sensors have broad application prospects, such as human motion monitoring and personalized recognition. However, their applicability is limited by complex structures, low output performance, low sensitivity, and narrow measurement range. In this study, we report a single-electrode spongy triboelectric sensor (SSTS) mainly composed of spongy composite multi-walled carbon nanotubes/polydimethylsiloxane (MWCNT/PDMS) film and conductive fabric, which can simultaneously generate contact electrification and electrostatic induction coupling in a single-electrode contact-separation mode. The SSTS combines the triboelectric effect, properties of doping material, and spongy porous structure (soft sugar as a sacrificial template). An SSTS with an MWCNT content of 10 wt% and a porosity of 64% exhibits high sensitivity, a wide measurement range, and excellent linearity. It also displays two sensitivity regions (slopes): 1.324 V/kPa from 1.5 to 28 kPa in the low-pressure range and 0.096 V/kPa from 28 to 316.5 kPa in the high-pressure range, with linearities of 0.980 and 0.979, respectively. Furthermore, the SSTS delivers a high-performance output and high stability, thus enhancing the monitoring of hand pressure changes, human movement, personalized spatial recognition, and other detection tasks. This new strategy for human motion monitoring shows great potential in the healthcare fields, sports rehabilitation, and human-computer interactions.

triboelectric nanogenerator, spongy pressure sensor, single-electrode, high sensitivity, wide measurement range

Citation: Xie X, Hou X J, Qian S, et al. Wide measurement range and high sensitivity spongy MWCNT/polydimethylsiloxane pressure sensor based on a single-electrode enhanced triboelectric nanogenerator. Sci China Tech Sci, 2023, 66: 1734–1745, https://doi.org/10.1007/s11431-022-2362-y

1 Introduction

The rapidly developing "Internet of Things" technology [1,2] has revolutionized applications in healthcare [3,4], personalized recognition [5], motion monitoring [6], and human-computer interactions [7]. Although the performance of traditional flexible pressure sensors has greatly improved, the complex structure, low sensitivity, narrow measurement range, power supply difficulty, and high cost of these sensors remain problematic [8–10]. Current flexible pressure sensors are generally classified into four different working mechanisms (triboelectric effect [11,12], piezoelectric effect [13], capacitance effect [14], and piezoresistive effect [15]). In triboelectric sensors, contact electrification is coupled with electrostatic induction to convert an applied pressure into an electrical signal [16]. Triboelectric sensors have met various expectations. A triboelectric sensor can be doped to change its electrical output performance [17], and its specific surface area can be increased to improve its sensitivity [12,18]. Consequently, these sensors are potentially available for the analysis and application of electrical signals generated under different external stimuli.

*Corresponding authors (email: drhejian@nuc.edu.cn; houxiaojuan@nuc.edu.cn)

Most of the sensors based on triboelectric nanogenerators (TENGs) use a contact-separation method with a spacing structure [1], which mainly consists of a pair of positive and negative triboelectric surfaces and two corresponding sensing electrodes. This structure requires many layers and a complex preparation process [19,20]. TENGs can be directly connected to any material (such as acrylic sheet materials, nitrile glove materials, and wear-resistant rubber materials in single-electrode working mode) and placed at any location for applications. Therefore, they solve the problems of complex structure, poor stability, and single-contact materials [21,22]. Polydimethylsiloxane (PDMS) is the most commonly used TENG base of tribo-materials as it offers excellent flexibility [23], high electronegativity [24], non-toxicity, thermal stability [25], and other superior properties. The dielectric properties of PDMS composite films can be improved by mixing nanoparticles with a high dielectric constant [26,27]. In recent years, high specific surface area and improved electrical output characteristics have been achieved by changing the surface or internal structure of a triboelectric film. However, the typical solutions—micropattern pyramid arrays [28], electrostatic spinning [29], microneedles [30], nanowires/microwires [31,32], and other structures—require processes such as photolithography and etching, which greatly increase the production cost and preparation difficulty.

In this work, we present a low-cost sensor with a simple structure. When spongy composite multi-walled carbon nanotubes (MWCNTs) are doped into PDMS with soft sugar as a sacrificial template, an external force triggers contact electrification between the exposed MWCNTs in the inner cavity and the PDMS matrix on the inner surface. Besides improving the electrical output performance, the proposed method increases the specific surface area of the film, achieving excellent electrical output performance, high sensitivity, and a wide measuring range. When the MWCNT content is 10 wt%, and the porosity reaches 64%, the single-electrode spongy triboelectric sensor (SSTS) has a wide measuring range (1.5–316.5 kPa), high sensitivity (sensitivity: 1.324 V/kPa, linearity: 0.986 in the low-pressure zone (1.5–28 kPa); sensitivity: 0.096 V/kPa, linearity: 0.979 in the high-pressure zone (28–316.5 kPa)), and excellent durability and stability (over 7000 cycles). The effects of MWCNT content, porosity, and size on the output performance of the SSTS are also investigated. These characteristics enable monitoring of hand pressure changes, human motion movement, and personalized spatial recognition, thereby widening the application range of SSTS in healthcare, motion monitoring, and human-computer interactions.

2 Experimental section

2.1 Materials and fabrication

MWCNTs were purchased from Kaisa (Guangdong) New Materials Co., Ltd. (Guangdong, China). PDMS elastomer and curing agent (Sylgard 184) were purchased from Dow Corning. Soft sugar was obtained from Shanghai Yishen Health Care Food Co., Ltd. (China). Ethanol (≥99.7%) was purchased from Chengdu Chemical Co., Ltd. (China). Double-sided conductive fabric tape (3J) and three-dimensional (3D) printer mold (for models with the same contact area (2 cm × 2 cm) and different thicknesses (1.65, 2.00, 2.50, 3.00, 4.50, and 5.50 mm)) were obtained from Zhejiang Chuanyin Technology Co., Ltd. (China).

The MWCNT/PDMS spongy composite films were fabricated through the following steps. (1) The MWCNTs (0.33 g) and PDMS (3 g) were mixed at a mass ratio of 10 wt% (500 r/min, 30 min). (2) Ethanol and the sacrificial template (soft sugar of different porosities, controlled by adjusting the added mass) were added to the MWCNT/PDMS substrate and stirred at 500 r/min for 1 h. (3) The mixture was placed in an oven (BAIHUI electric heating blast-drying oven, China) and heated at 80°C. The amount of remaining ethanol was observed at 15-min intervals to ensure that all ethanol was completely evaporated. (4) A curing agent (1:10 weight ratio of curing agent to PDMS) was added to the mixture (500 r/min, 30 min). (5) The prepared mixture was poured into the mold, then left in the mold for 2 h to remove internal air bubbles. (6) The mold was placed on the heating table at 90°C for 1 h until the mixture was completely cured. (7) The cured mixture was immersed in water and heated at 85°C for 90 min. During the heating process, the water was changed every 30 min to ensure the complete removal of the residual soft sugar. (8) The films were placed in a dryer oven and dried at 80°C for 4 h to remove water from their spongy structures. Finally, we obtained the prepared spongy composite MWCNT/PDMS films.

To fabricate the SSTSs, the prepared SSTSs were cut into the appropriate shapes and sizes for specific situations. They were easily assembled by combining a conductive fabric (a 2 cm by 2 cm electrode layer) with the spongy composite MWCNT /PDMS film (triboelectric layer).

2.2 Characterization and measurement

The surface morphologies of the flat composite MWCNT/PDMS film, the spongy composite MWCNT/PDMS film, soft sugar, and the MWCNTs were characterized using field-emission scanning electron microscopy (SEM) (TESCAN MIRA LMS, Czech). X-ray diffraction (XRD) analysis was carried out on a DX-2700X X-ray diffractometer (Dandong Fangyuan Instrument Co., Ltd., China). The output voltage and current were measured with a Keithley 2611B electrometer system and a Tektronix MSO 2024B Mixed Signal Oscilloscope. The generated data were collected and analyzed via the LabVIEW programming interface, allowing real-time data acquisition and analysis. For quantitative

measurement, the SSTS was fixed on a linear motor. The magnitude of the applied force was measured on a pressure-sensing test system comprising an HZC-T-300N pressure sensor and an LZ-808 monitor (both purchased from Bengbu Chengying Sensor Co., Ltd., China).

3 Results and discussion

This paper presents the design and fabrication of an SSTS based on the spongy composite MWCNT/PDMS film. Figure 1(a) is a schematic of the fabricated and assembled SSTS array. The main manufacturing process of the SSTS based on the sacrificial template method is shown in Figure S1, and the preparation process is detailed in the Experimental section. The SSTS has a simple structure and is prepared by an easy process. Its main constituents are the conductive fabric (electrode layer) and the spongy composite MWCNT/PDMS film (triboelectric layer). Figure 1(b) and (c) are SEM images of the soft sugar and MWCNTs, respectively, at different magnifications. The fondant is approximately 200–500 μm in diameter, and the morphology of the MWCNTs is visible only at the higher magnification (scale bar = 2 μm). The MWCNTs are further confirmed in the right images of Figure 1(d) and (e), which show locally magnified SEM images of the flat 10 wt% MWCNT/PDMS film and the spongy

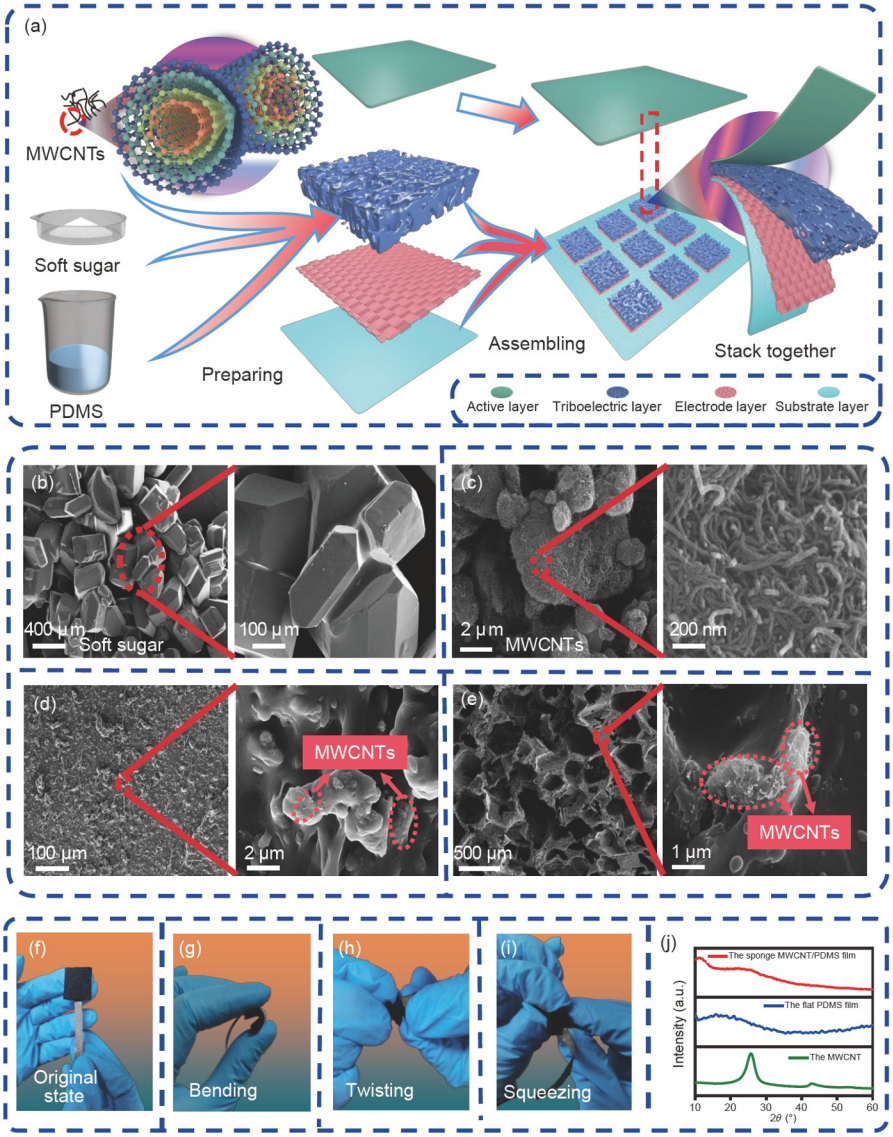

Figure 1 (Color online) SSTS fabrication process and characterization. (a) Schematic of the fabricated and assembled SSTS array; (b), (c) SEM images of soft sugar and MWCNTs (the right images are magnified views of the regions enclosed in ovals on the left images); (d), (e) cross-sectional SEM images of the flat and spongy composite MWCNT/PDMS films (the right images are magnified views of the regions enclosed in ovals on the left images, along with labels of the exposed MWCNTs); (f)–(i) photographs of the SSTS under different deformations; (j) XRD patterns of the spongy composite MWCNT/PDMS film, the flat PDMS film, and the MWCNTs.

composite 10 wt% MWCNT/PDMS film with 64% porosity. The exposed MWCNTs in these images are labeled (see Figure S2 for details). To increase the dielectric constant and specific surface area and hence optimize the output performance, sensitivity, and measurement range, the spongy composite MWCNT/PDMS film mainly combines a high dielectric constant material with a spongy porous structure. The SSTS is flexible and stable under different deformations (see the photographs in Figure 1(f)–(i)). Figure 1(j) shows XRD patterns of the spongy composite MWCNT/PDMS film, flat PDMS film, and MWCNTs. The two strong diffraction peaks of MWCNTs, observed at 25.8° and 42.9°, are associated with the (002) and (100) crystal faces, respectively [33]. The diffraction peak at 15.9° corresponds to PDMS microcrystals, and the MWCNT/PDMS diffraction peaks appear at 11.6° and 23.9°. However, the diffraction peak of MWCNT disappears in the composite film, possibly because the MWCTs are uniformly dispersed through the PDMS, so their diffraction intensity is completely covered by the PDMS matrix [34].

Figure 2(a) shows the power generation mechanism of the prepared SSTS. The details of this mechanism are shown in Figure 2(b) and Figure S4. The triboelectric layer is a spongy composite MWCNT/PDMS film, the electrode layer at the bottom is a conductive fabric, and the active layer is an acrylic plate, a nitrile glove, or a wear-resistant rubber

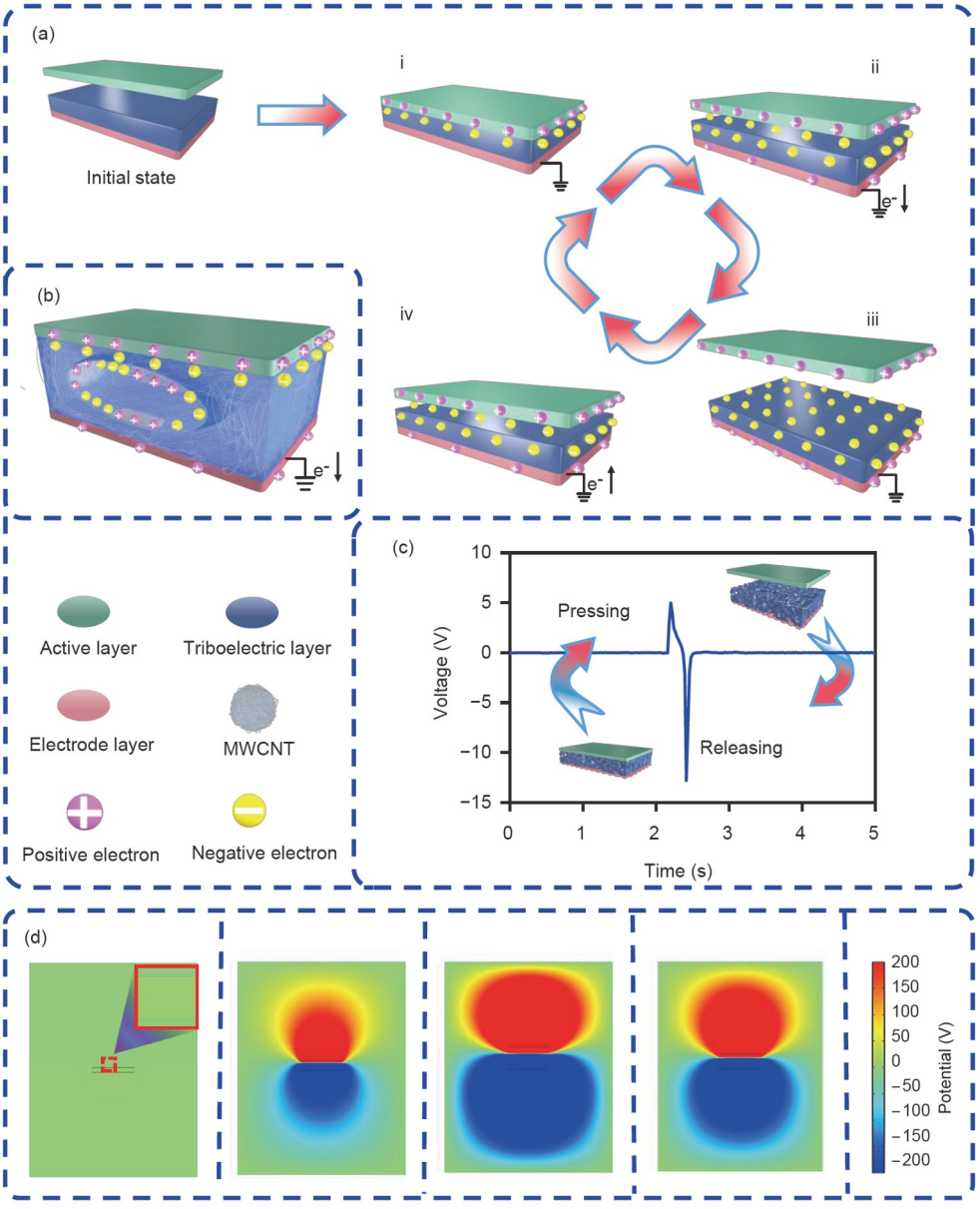

Figure 2 (Color online) Schematics of the SSTS. (a) Electricity generation process through a full cycle of the SSTS under an external force; (b) SSTS electricity generation process released in contact-separation mode; (c) one cycle of the open-circuit voltage output from the SSTS; (d) COMSOL potential simulation to elucidate the working principle.

material. In single-electrode mode, the internal pores of the MWCNT/PDMS film are subjected to an external force, causing the exposed MWCNTs and PDMS matrix to form an internal contact-separation mode. Figure S3 schematizes the data acquisition and processing system for directly testing the performance output of the flexible SSTS. This contact-separation mechanism relies mainly on the working principles of triboelectric and electrostatic induction [35]. The analysis starts from the original state (Figure 2(a)) when the active layer applies an external force on the spongy composite MWCNT/PDMS triboelectric layer. At this time, the triboelectric layer completely contacts the active layer. As the resulting charges of opposite polarity are perfectly balanced, no electrons flow to the external circuit (i). Once the external force is stopped, the active layer begins to separate from the spongy composite film, and the interacting surfaces have opposite triboelectric charges. The negative charge on the surface of the spongy composite film induces a positive charge on the electrode layer. Free electrons then flow from the electrode layer to the ground, resulting in an output current signal (ii). When the spongy composite film completely separates from the active layer, the SSTS reaches a charge-equilibrium state, and no output signal is observed (iii). As the spongy composite film moves toward the active layer, electrons begin moving toward the electrode layer, resulting in a reverse output current signal (iv). When the spongy composite film and the active layer again overlap, the potential returns to its original state. The output signal generation process of a single SSTS is a complete cycle. In periodic contact-separation mode, a periodic alternating voltage in the same phase is generated in the external circuit, as shown in Figure 2(c). The potential distributions of the SSTS in four different states were simulated using COMSOL. The results are shown in Figure 2(d).

We now discuss the effects of a series of key parameters (content, porosity, and size of the MWCNTs in SSTS) on the previously mentioned electrical output of the SSTS. The MWCNT content greatly influences the electrical output. In a flat composite film (2 cm × 2 cm × 3 mm) containing 10 wt% MWCNTs and an active layer of acrylic sheet material, the measured optimal outputs of open-circuit voltage (V_{oc}) and short-circuit current (I_{sc}) under a periodic 108 N force were 138 V and 3.37 μA, respectively, 2.82 and 2.96 times higher than those of undoped flat PDMS (Figure 3(a) and (b)). The V_{oc} and I_{sc} trended similarly with MWCNT content, as shown in Figure 3(c).

The high electrical performance is mainly attributable to the improved dielectric constant of the composite film doped with different contents of MWCNTs. According to Lichtenecker's logarithmic mixture formula [27,36,37], the effective dielectric constant of the composite film is

$$\varepsilon_{\text{eff}} = \varepsilon_{\text{a}} f_{\text{a}} + \varepsilon_{\text{b}} f_{\text{b}}, \tag{1}$$

where ε_{a} and f_{a} represent the permittivity and volume fraction of the doped MWCNTs, respectively, and ε_{b} and f_{b} represent the permittivity and volume fraction of PDMS, respectively. In general, the higher the dielectric constant ($\varepsilon_{\text{eff}} > \varepsilon_{\text{b}}$) of composite films, the better the output performance because increasing the dielectric constant changes the maximum transferred charge density δ', which can be expressed as

$$\delta' = \frac{\delta_0 d}{d + h/\varepsilon_{\text{eff}}}, \tag{2}$$

where δ_0 is the density of the triboelectric charge at equilibrium, d is the distance between the triboelectric and active layers, and h is the thickness of the MWCNT/PDMS composite film. However, the output performance decreases significantly when the MWCNT content exceeds 10 wt%. Excess MWCNT content increases the agglomeration and particle accumulation on the material surface, thereby reducing the effective contact area of the composite film and decreasing the surface charge density. As shown in Figure 3 (d) and (e), the porosity P is another important influencer of the electrical output performance of SSTS. The porosity P, controlled by adding different qualities of soft sugar, was calculated by the following equations [22,26,38]:

$$P = \frac{V_{\text{void}}}{V_{\text{nonporous}}} = \frac{V_{\text{nonporous}} - V_{\text{porous}}^{\text{air}}}{V_{\text{nonporous}}} \times 100\%, \tag{3}$$

$$V_{\text{nonporous}} = \frac{M_{\text{nonporous}}}{\rho_{\text{nonporous}}}, \tag{4}$$

$$V_{\text{porous}}^{\text{air}} = \frac{M_{\text{porous}}}{\rho_{\text{porous}}}, \tag{5}$$

$$P = \frac{M_{\text{nonporous}} - M_{\text{porous}}}{M_{\text{nonporous}}} \times 100\%, \tag{6}$$

$$P = \frac{F}{S}, \tag{7}$$

where $V_{\text{nonporous}}$ is the volume of the flat composite MWCNT/PDMS film; additionally, the volume of the spongy composite porous MWCNT/PDMS film prepared in the same mold cavity. $V_{\text{porous}}^{\text{air}}$ is the volume occupied by pores in the spongy composite MWCNT/PDMS film, and M_{porous} and $M_{\text{nonporous}}$ are the weights of the spongy composite MWCNT/PDMS film and flat composite MWCNT/PDMS film, respectively. ρ_{porous} and $\rho_{\text{nonoporous}}$ are spongy and flat composite MWCNT/PDMS films, respectively, with the same density [26]. From eqs. (3)–(6) and the experimental results, one observes that when the MWCNT content is 10 wt%, the mass of SSTS is 0.65 g (2 cm × 2 cm × 4.5 mm) and the porosity is 64%, the optimal outputs V_{oc} and I_{sc} of the corresponding SSTS are 1.85 and 1.52 times higher than those of the doped flat composite MWCNT/PDMS film,

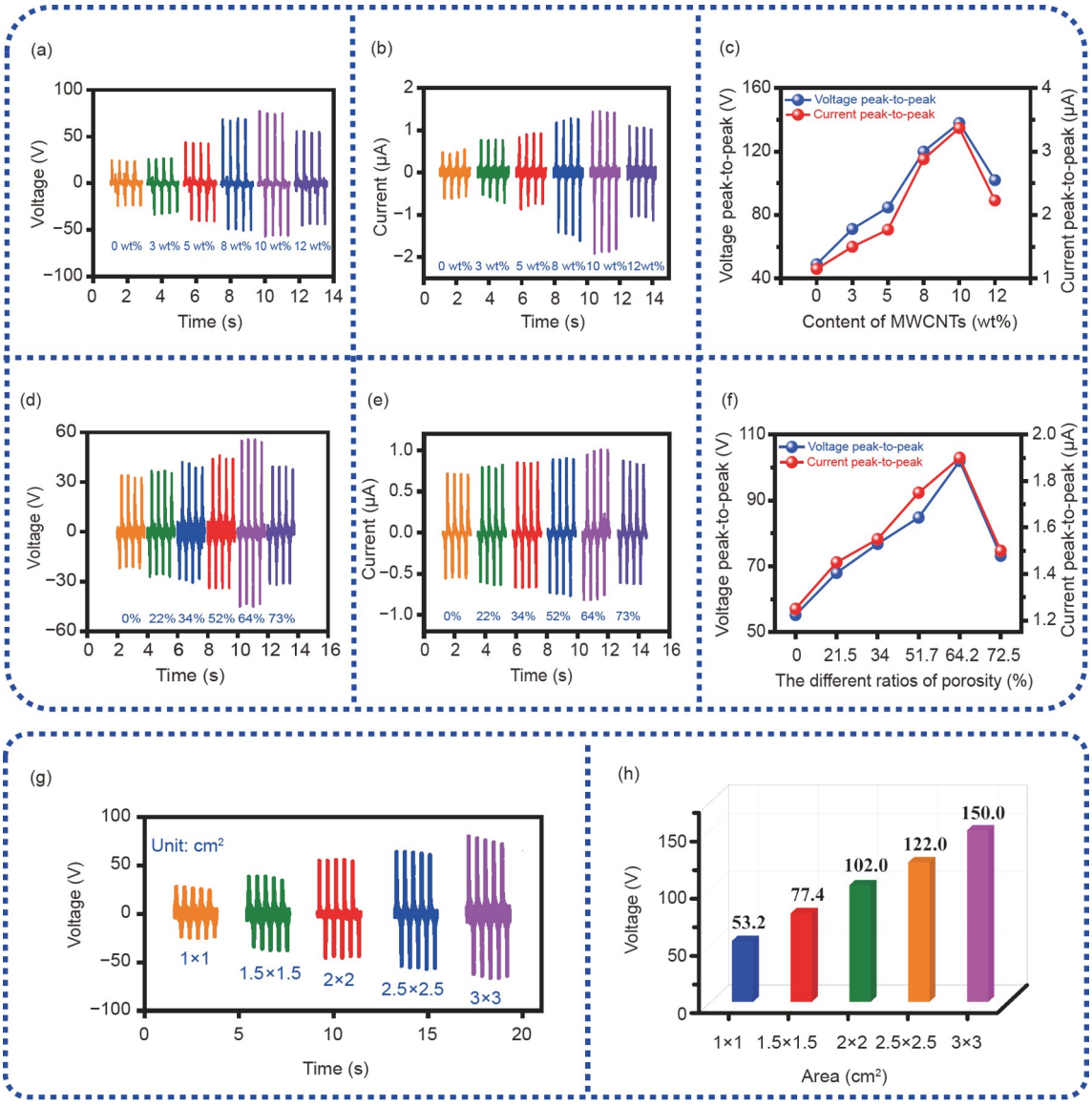

Figure 3 Impacts of MWCNT, porosity, and dimensions on the electrical output of SSTS. (a)–(c) Electrical outputs of SSTSs (2 cm × 2 cm × 3 mm) with different mass ratios of MWCNT (0–12 wt%); (d)–(f) electrical outputs of SSTSs with constant MWCNT content (10 wt%), constant SSTS mass (0.65 g; 2 cm × 2 cm) and different porosities (0–73%); (g) voltage outputs of SSTSs with different lateral areas (1 cm × 1 cm to 3 cm × 3 cm) (MWCNT content = 10 wt%, porosity = 64%); (h) maximum voltage outputs of SSTSs with different areas.

respectively. As the porosity varied, the obtained V_{oc} and I_{sc} showed similar trends (Figure 3(f)). As the porosity increases, the internal surface area increases, thereby increasing the electrical output. However, if the porosity becomes excessively high, the wall thickness between the pores becomes too thin to recover the deformation of the cavity, so the structure deforms irreversibly under a repeatedly applied external force. The electrical output then decreases. As the measured length of the sample size increases in 0.5-cm increment (Figure 3(g)), the electrical output of the SSTS shows an increasing trend (Figure 3(g) and (h), and Figure S5), and the voltage output shows a linear enhancement with a linearity of 0.980 (Figure S6). Intuitively, this result indicates that the measured electrical output depends on the size of the SSTS. In addition, the output voltage increases with film thickness (Figure S7). The above results demonstrate that the electrical output depends on the SSTS volume; moreover, they strongly prove that the electrical output comes from the inner cavity.

To explore the pressure response of the SSTS (2 cm × 2 cm), the output voltage of the device was measured using a linear motor under different cyclic force conditions. The results are shown in Figure 4(a) and (b). The force applied by the linear motor ranges from 1.5 to 316.5 kPa (0.6 to 126.6 N). The unit conversion formula between N and kPa is given by where P refers to the pressure per unit area of film, and F and S are the applied external force and contact area of the film, respectively. As shown in Figure 4(a) and (b), the

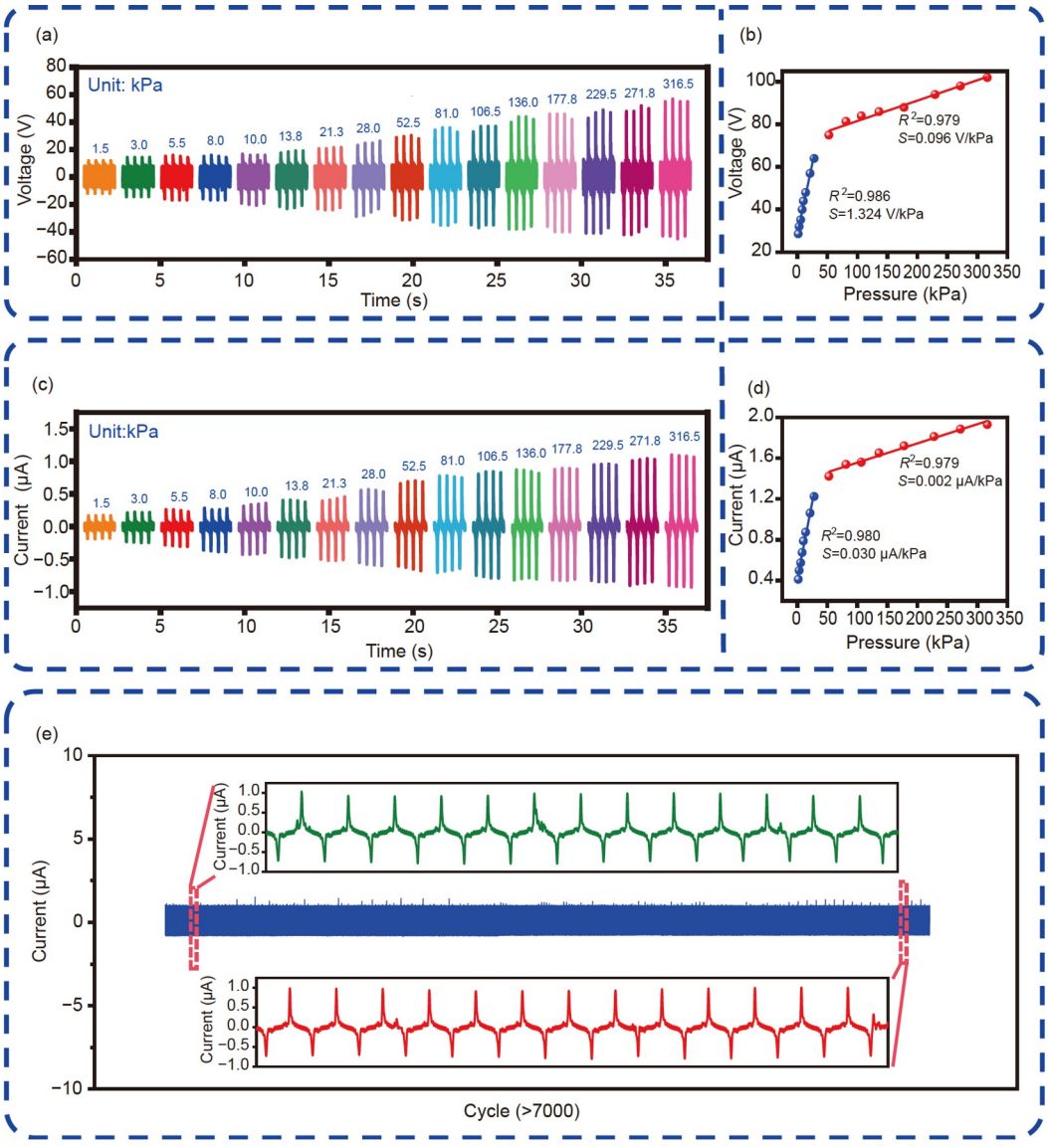

Figure 4 (Color online) Characterization of the electrical properties of SSTS. (a) Output voltage of the SSTS under different impact pressures; (b) results of linear fitting analysis calculated from (a); (c) output voltage current of the SSTS under different impact pressures; (d) results of linear fitting analysis calculated from (c); (e) stability testing of SSTS (showing enlargement during cyclic testing).

electric output V_{oc} of the SSTS increases by 3.57-fold (from 28.6 to 102 V) as the pressure increases from 1.5 to 316.5 kPa. Meanwhile, the sensor's electrical output I_{sc} increases by 4.68-fold, from 0.412 to 1.930 μA (Figure 4(c)). Linearity and sensitivity are important measurement indices of sensors. As seen in Figure 4(b), the voltage sensitivity of the SSTS is divided into two sensitivity regions over the wide measurement range (1.5–316.5 kPa): One in the low-pressure range (1.5–28 kPa) with a sensitivity of 1.324 V/kPa, the other in the high-pressure range (28–316.5 kPa) with a sensitivity of 0.096 V/kPa. The sensitivity and linearity of the output current are shown in Figure 4(d). The sensitivity is 0.030 μA/kPa in the range of 1.5–28 kPa and 0.002 μA/kPa in the range of 28–316.5 kPa, with linearities of 0.980 and 0.979, respectively. Note that the sensitivities differ between these two ranges (1.5–28 kPa and 28–316.5 kPa). Although the output voltage and current increase proportionally in both the low-voltage and high-voltage regions, their growths are relatively slow when the applied force exceeds 28 kPa. This result can be explained by the pores of the composite sponge film in the triboelectric material. In the low-pressure region (1.5–28 kPa), when the force is small, the pores are incompletely closed, but in the high-pressure region (28–316.5 kPa) when the force is large, the pores are completely closed, so the linearity slope decreases. Moreover, the power-output performance of the device is maintained over more than 7000 cycles under a force of 108 N (Figure 4(e)). Even after thousands of cycles, the power output almost retains its initial value, ensuring the stable output performance of this sensor. Meanwhile, the

response time is 23 ms (Figure S8), providing strong support for high-resolution monitoring by the SSTS. These values outperform most of the previously reported pressure sensors listed in Table 1, demonstrating the superior performance characteristics of this pressure sensor.

In daily work, our hands are often engaged in pressing a computer mouse. Video S1 shows real-time monitoring of the SSTS (2 cm × 2 cm × 4.5 mm with an active layer of nitrile glove material; Figure 5(a)). The output details reveal the voltage-output differences among three different types of mouse pressing: heavy tapping, mid-level tapping, and light tapping. This sensor clearly recognizes the three different mouse-press modes. Furthermore, it can monitor the pressure on the hand and distinguish different forces (Figure 5(b) and Video S2) to determine the activity of the metacarpal muscles and wrist joints, which is useful for rehabilitation and detection. This pressure sensor can also effectively detect various human-movement conditions. Figure 5(c) and Video S3 demonstrate the SSTS (2 cm × 2 cm × 4.5 mm with an active layer of wear-resistant rubber material) monitoring five different human-movement patterns: multiple tests of jiggling feet, walking, jogging, running, and jumping. The SSTS shows high repeatable detection capability. Furthermore, detailed motion information can be distinguished from the vibration amplitudes, time intervals, and waveform shapes of adjacent individual waveforms. Figure 5(d) displays the statistical results of different motion states and enlarged views of each of the five modes. Its *X* and *Y* axes represent the vacate time and the ground time, respectively (the vacate time is represented as the time interval of adjacent peaks, and the ground time is represented as the time interval of adjacent cycles, Figure S9). The raw data are provided in Table S1. The gait frequencies of different movements are also accurately obtained (Figure 5(e)). The SSTS provides a very promising external sensing function that can accurately determine and distinguish various motion modes based on their voltage waveforms, frequencies, and times. Especially in the sports fields [20,43], the sensor can be used for accurately analyzing the monitoring data of human movements. Therefore, it can assist sports coaches and physiotherapists in developing various training plans and competition strategies suitable for different individuals, thus helping athletes to improve their performance within a short time. It can also help patients with mobility difficulties requiring specialized rehabilitation training. The sensor has a wide range of applications in healthcare and motion monitoring scenarios.

The pressure sensing array consists of a 3 × 3 arrangement of single-electrode triboelectric sensors with an additional support layer at the bottom of the sensors. This array is useful for studying multi-touch stimulation and personalized spatial recognition (Figure 6(a); also Figure S10 for an optical image and detailed section of the triboelectric sensor array). Each pixel from P_{11} to P_{33} is marked. Each time it slides along the same path, the electrical output of the contacted pixel enlarges while the untouched pixel outputs only noise signals. Based on this principle, the motion trajectory of the active layer can be monitored. The signal at P_{13}, where the finger slides along the same path, was measured using the 2611B data measurement system (Video S4). The specific finger-movement position is shown in Figure 6(c) and Figure S11(b) and (c). The waveform, columnar, and fitted surface

Table 1 Performance comparison of different pressure sensors

Material[a)]	Electrode	Measurement range	Sensitivity	Response time (ms)	Stable cycles	Sensing mechanism	Reference
TPU/PVDF-HFP nanofibers, liquid metal, Al, and PTFE	Double-electrode	90–400 kPa	0.071 V/kPa	86	1000	Capacitance sensor	[8]
PP, copper, and PTFE	Double-electrode	6.25–31.25 kPa 31.25–112.5 kPa	0.86 V/kPa 0.15 V/kPa	/	50000	Triboelectric sensor	[39]
PET, graphene, acrylic, and PDMS	Single-electrode	10.6–101.7 kPa	0.274 V/kPa	/	2000	Triboelectric sensor	[40]
Carbon, PDMS, and $BaTiO_3$/GFF-PVDF	Double-electrode	0–10 N	3.31 V/kPa	19	3000	Piezoelectric sensor	[10]
Mxene/cotton fabric, PDMS, and PI	Interdigital electrodes	0–1.30 kPa 1.30–10.25 kPa 10.25–40.73 kPa 40.73–160 kPa	$5.30\ kPa^{-1}$ $2.27\ kPa^{-1}$ $0.57\ kPa^{-1}$ $0.08\ kPa^{-1}$	50	>1000	Piezoresistive sensor	[41]
PVDF/MXene nanofibers, conductive fabric, and nylon	Single-electrode	0–5 kPa 5–16 kPa	12.33 V/kPa 3.72V/kPa	70	16000	Triboelectric sensor	[9]
Carbonized crepe paper, silver paste, and PI	Interdigital electrodes	0–0.42 kPa 0.42–2.53 kPa 2.53–9.06 kPa 9.06–20 kPa	$5.67\ kPa^{-1}$ $2.52\ kPa^{-1}$ $10.87\ kPa^{-1}$ $0.32\ kPa^{-1}$	<30	>3000	Resistive sensor	[42]
MWCNT/PDMS, acrylic sheet, and conductive fabric	Single-electrode	1.5–28 kPa 28–316.5 kPa	1.324 V/kPa 0.096 V/kPa	23	>7000	Triboelectric sensor	This work

a) TPU/PVDF-HFP, thermoplastic polyurethanes/poly(vinylidene fluoride-co-hexafluoropropylene); PTFE, polytetrafluoroethylene; PP, polypropylene; PI, polyimide.

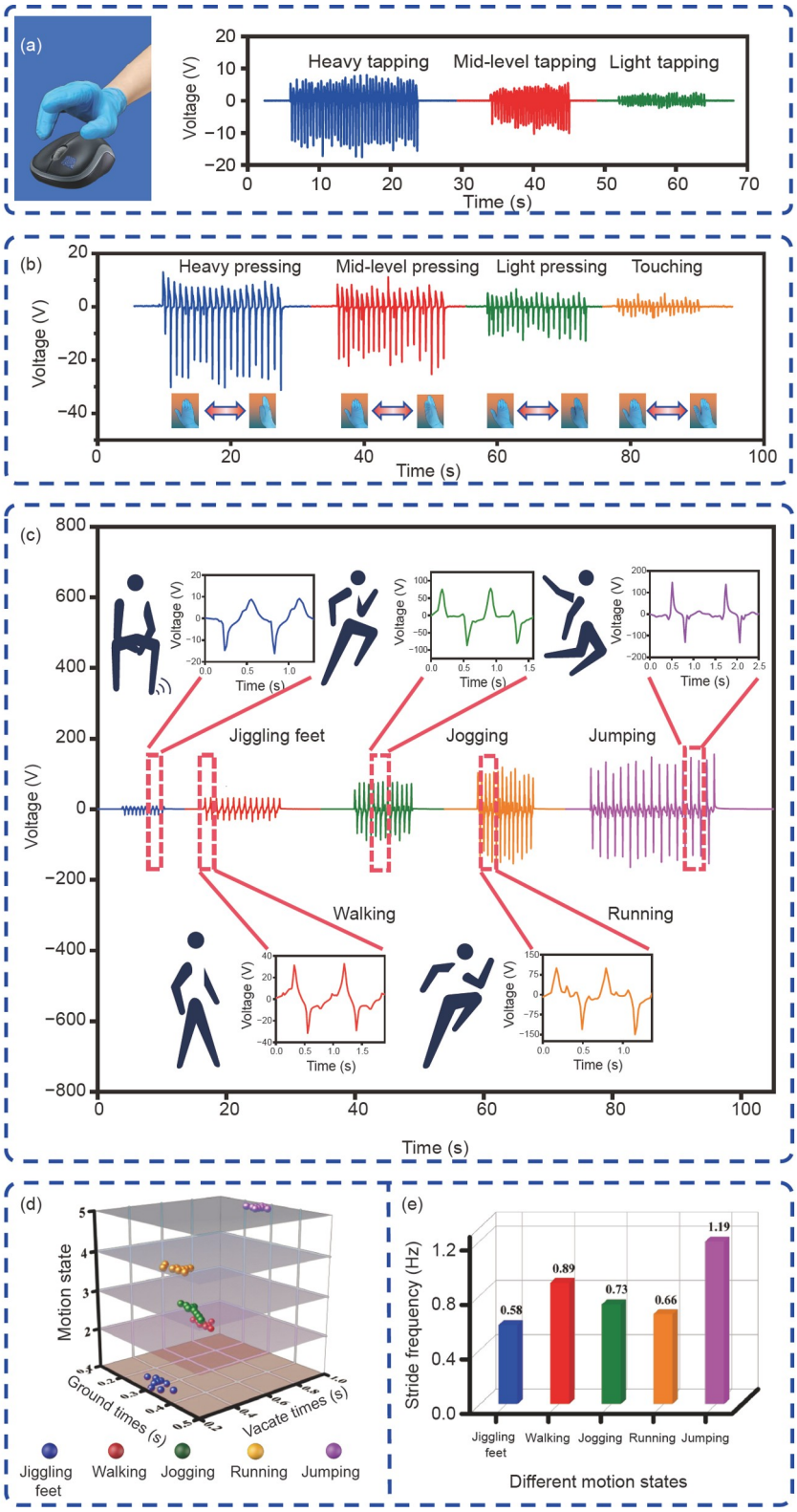

Figure 5 (Color online) Potential applications of SSTS. (a) Output voltage curves of mouse pressing in three different modes; (b) output voltage curves of SSTS pressed in four different modes; (c) SSTS signal feedback to the human motion state and outputs under five different motion states; (d) comparative analysis of different exercise-time intervals; (e) step frequency statistics of different actions.

electrical outputs of three different trajectories ("I," "C," and "Z") are shown in Figure 6(b) and (d) and Figure S11(a), respectively. Trajectory recognition by the 3 × 3 SSTS arrays can be extended to the near-sidelines of ball sports such as

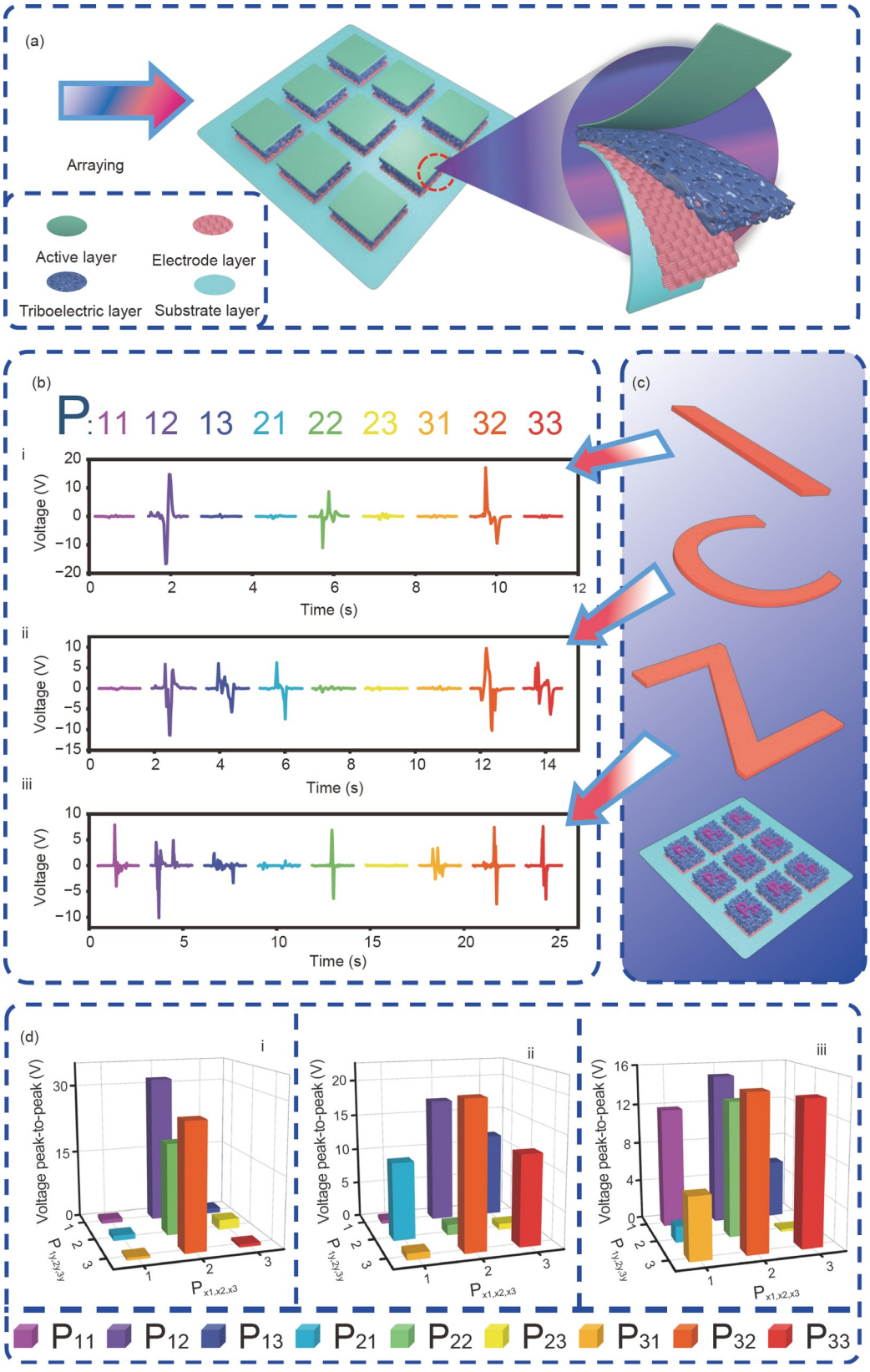

Figure 6 (a) Schematic representation of the SSTS 3 × 3 array structure and a magnified view of an individual SSTS; (b), (d) outputs of SSTS array under different sliding trajectories; (c) detailed arrangement of pixels P_{11} to P_{33} in the SSTS array and the sliding track.

tennis, badminton, and table tennis [43], along with other scenarios requiring the use of "eagle eyes." Of course, the sensor can also identify the pressure distribution of different personalized spaces, and its specific application scenarios

can be customized to users' needs. In summary, the SSTS presents superior external-force sensing performance via the conversion of external mechanical properties to electrical signals. The sensor can potentially revolutionize healthcare, sports rehabilitation, personal recognition, human-computer interactions, and other areas.

4 Conclusion

Based on the coupling effect of triboelectric and electrostatic induction, we proposed a novel fabrication process of a self-powered single-electrode spongy triboelectric sensor from composite MWCNT/PDMS materials. The fabricated SSTS demonstrates good flexibility, durability, and stability. The electrical output of the spongy composite MWCNT/PDMS film significantly exceeds those of an undoped flat PDMS film and a flat composite MWCNT/PDMS film. The SSTS is a flexible pressure sensor with high sensitivity and a wide measurement range. In the pressure ranges of 1.5–28 kPa and 28–316.5 kPa, the sensitivities are 1.324 and 0.096 V/kPa, respectively, with corresponding linearities of 0.986 and 0.979, respectively. By virtue of MWCNT doping and a porous structure, the open-circuit voltage output of the single-electrode sponge composite MWCNT/PDMS is 2.82 and 1.85 times higher, respectively, than that of the undoped and flat films. Meanwhile, the short-circuit current output shows the same increasing trend. This flexible pressure sensor recognizes mouse clicks, hand presses, and human movements and further realizes personalized spatial recognition. These demonstrations suggest a wide range of applications in healthcare, motion monitoring, personalized recognition, human-computer interactions, and other fields.

This work was supported in part by the National Key Research and Development Program of China (Grant No. 2019YFB2004802), the National Natural Science Foundation of China (Grant Nos. 62171414, 52175554, 52205608, 62171415 & 62001431), the Fundamental Research Program of Shanxi Province (Grant Nos. 20210302123059 & 20210302124610), and the Program for the Innovative Talents of Higher Education Institutions of Shanxi.

1 Zhang J, Zhang Y, Li Y, et al. Textile-based flexible pressure sensors: A review. Polym Rev, 2022, 62: 65–94
2 Wang B, Facchetti A. Mechanically flexible conductors for stretchable and wearable E-skin and E-textile devices. Adv Mater, 2019, 31: 1901408
3 Shabbir I, Rubab N, Kim T W, et al. Healthcare management applications based on triboelectric nanogenerators. APL Mater, 2021, 9: 060703
4 Wang C, Shi Q, Lee C. Advanced implantable biomedical devices enabled by triboelectric nanogenerators. Nanomaterials, 2022, 12: 1366
5 Jiang X, Chen R, Zhu H. Recent progress in wearable tactile sensors combined with algorithms based on machine learning and signal processing. APL Mater, 2021, 9: 030906
6 Lou M, Abdalla I, Zhu M, et al. Hierarchically rough structured and self-powered pressure sensor textile for motion sensing and pulse monitoring. ACS Appl Mater Interfaces, 2020, 12: 1597–1605
7 Yu J, Xian S, Zhang Z, et al. Synergistic piezoelectricity enhanced $BaTiO_3$/polyacrylonitrile elastomer-based highly sensitive pressure sensor for intelligent sensing and posture recognition applications. Nano Res, 2023, 16: 5490–5502
8 Uzabakiriho P C, Wang M, Ma C, et al. Stretchable, breathable, and highly sensitive capacitive and self-powered electronic skin based on core-shell nanofibers. Nanoscale, 2022, 14: 6600–6611
9 Xu H, Tao J, Liu Y, et al. Fully fibrous large-area tailorable triboelectric nanogenerator based on solution blow spinning technology for energy harvesting and self-powered sensing. Small, 2022, 18: 2202477
10 Zhou P, Zheng Z, Wang B, et al. Self-powered flexible piezoelectric sensors based on self-assembled 10 nm $BaTiO_3$ nanocubes on glass fiber fabric. Nano Energy, 2022, 99: 107400
11 He H C, Mu J L, Mu J B, et al. Breeze-activated wind speed sensor with ultra-low friction resistance for self-powered gale disaster warning. Sci China Tech Sci, 2023, 66: 57–70
12 Yu J, Hou X, Cui M, et al. Highly skin-conformal wearable tactile sensor based on piezoelectric-enhanced triboelectric nanogenerator. Nano Energy, 2019, 64: 103923
13 Wang D, Zhang D, Li P, et al. Electrospinning of flexible poly(vinyl alcohol)/mxene nanofiber-based humidity sensor self-powered by monolayer molybdenum diselenide piezoelectric nanogenerator. Nano-Micro Lett, 2021, 13: 57
14 Mishra R B, El-Atab N, Hussain A M, et al. Recent progress on flexible capacitive pressure sensors: From design and materials to applications. Adv Mater Technol, 2021, 6: 2001023
15 Wang Z, Liu Z, Zhao G, et al. Stretchable unsymmetrical piezoelectric $BaTiO_3$ composite hydrogel for triboelectric nanogenerators and multimodal sensors. ACS Nano, 2022, 16: 1661–1670
16 Wu B, Zhang Z X, Xue X B, et al. A stretchable triboelectric generator with coplanar integration design of energy harvesting and strain sensing. Sci China Tech Sci, 2022, 65: 221–230
17 Mu J, Zou J, Song J, et al. Hybrid enhancement effect of structural and material properties of the triboelectric generator on its performance in integrated energy harvester. Energy Convers Manage, 2022, 254: 115151
18 Ouyang H, Tian J, Sun G, et al. Self-powered pulse sensor for antidiastole of cardiovascular disease. Adv Mater, 2017, 29: 1703456
19 Kim W G, Kim D W, Tcho I W, et al. Triboelectric nanogenerator: Structure, mechanism, and applications. ACS Nano, 2021, 15: 258–287
20 Rana M, Mittal V. Wearable sensors for real-time kinematics analysis in sports: A review. IEEE Sens J, 2021, 21: 1187–1207
21 Wang M, Zhang N, Tang Y, et al. Single-electrode triboelectric nanogenerators based on sponge-like porous PTFE thin films for mechanical energy harvesting and self-powered electronics. J Mater Chem A, 2017, 5: 12252–12257
22 Cui C, Wang X, Yi Z, et al. Flexible single-electrode triboelectric nanogenerator and body moving sensor based on porous Na_2CO_3/polydimethylsiloxane film. ACS Appl Mater Interfaces, 2018, 10: 3652–3659
23 Qu M, Shen L, Wang J, et al. Superhydrophobic, humidity-resistant, and flexible triboelectric nanogenerators for biomechanical energy harvesting and wearable self-powered sensing. ACS Appl Nano Mater, 2022, 5: 9840–9851
24 Wu J, Wang X, He J, et al. Synthesis of fluorinated polyimide towards a transparent triboelectric nanogenerator applied on screen surface. J Mater Chem A, 2021, 9: 6583–6590
25 Song P, Liu B, Liang C, et al. Lightweight, flexible cellulose-derived carbon aerogel@reduced graphene oxide/pdms composites with outstanding emi shielding performances and excellent thermal conductivities. Nano-Micro Lett, 2021, 13: 91
26 Wang Q, Chen A, Gu H, et al. Highly interconnected porous PDMS/CNTs sandwich sponges with anti-icing/deicing microstructured

surfaces. J Mater Sci, 2021, 56: 11723–11735
27 Chen J, Guo H, He X, et al. Enhancing performance of triboelectric nanogenerator by filling high dielectric nanoparticles into sponge pdms film. ACS Appl Mater Interfaces, 2016, 8: 736–744
28 Cui J, Zhang B, Duan J, et al. A micro-pressure sensing method based on the micropatterned electrodes filled with the microspheres. Materials, 2017, 10: 1439
29 Li Y, Xiao S, Luo Y, et al. Advances in electrospun nanofibers for triboelectric nanogenerators. Nano Energy, 2022, 104: 107884
30 Ke K H, Chung C K. High-performance Al-PDMS TENG teng with novel complex morphology of two-height microneedles array for high-sensitivity force-sensor and self-powered application. Small, 2020, 16: 2001209
31 Singer E K, Chang L, Calderón A A, et al. Clip-brazing for the design and fabrication of micronewton-resolution millimeter-scale force sensors. Smart Mater Struct, 2019, 28: 055028
32 Liu Y, Zhu L Y, Feng P, et al. Bimetallic AuPt alloy nanoparticles decorated on ZnO nanowires towards efficient and selective H_2S gas sensing. Sens Actuat B-Chem, 2022, 367: 132024
33 Kuziel A W, Dzido G, Turczyn R, et al. Ultra-long carbon nanotube-paraffin composites of record thermal conductivity and high phase change enthalpy among paraffin-based heat storage materials. J Energy Storage, 2021, 36: 102396
34 Wang Z, Li X, Wang L, et al. Flexible multi-walled carbon nanotubes/polydimethylsiloxane membranous composites toward high-permittivity performance. Adv Compos Hybrid Mater, 2020, 3: 1–7
35 Xiang H, Zeng Y, Huang X, et al. From triboelectric nanogenerator to multifunctional triboelectric sensors: A chemical perspective toward the interface optimization and device integration. Small, 2022, 18: 2107222
36 Hou X, Zhong J, Yang C, et al. A high-performance, single-electrode and stretchable piezo-triboelectric hybrid patch for omnidirectional biomechanical energy harvesting and motion monitoring. J Materiomics, 2022, 8: 958–966
37 Simpkin R. Derivation of lichtenecker's logarithmic mixture formula from Maxwell's equations. IEEE Trans Microwave Theor Techn, 2010, 58: 545–550
38 Fan Y J, Meng X S, Li H Y, et al. Stretchable porous carbon nanotube-elastomer hybrid nanocomposite for harvesting mechanical energy. Adv Mater, 2017, 29: 1603115
39 Xu J, Wei X, Li R, et al. A capsule-shaped triboelectric nanogenerator for self-powered health monitoring of traffic facilities. ACS Mater Lett, 2022, 4: 1630–1637
40 Lee Y, Kim J, Jang B, et al. Graphene-based stretchable/wearable self-powered touch sensor. Nano Energy, 2019, 62: 259–267
41 Zheng Y, Yin R, Zhao Y, et al. Conductive MXene/cotton fabric based pressure sensor with both high sensitivity and wide sensing range for human motion detection and E-skin. Chem Eng J, 2021, 420: 127720
42 Chen S, Song Y, Xu F. Flexible and highly sensitive resistive pressure sensor based on carbonized crepe paper with corrugated structure. ACS Appl Mater Interfaces, 2018, 10: 34646–34654
43 Luo J, Wang Z, Xu L, et al. Flexible and durable wood-based triboelectric nanogenerators for self-powered sensing in athletic big data analytics. Nat Commun, 2019, 10: 5147